THE JOURNAL OF PHYSICAL CHEMISTRY C

Article

pubs.acs.org/JPCC

Electronic Structure of Noncentrosymmetric α-GeO_2 with Oxygen Vacancy: Ab Initio Calculations and Comparison with Experiment

V. V. Atuchin,*[,†,‡] V. V. Kaichev,[§,∥] I. V. Korolkov,[⊥] A. A. Saraev,[§] I. B. Troitskaia,[†] T. V. Perevalov,[#] and V. A. Gritsenko[#]

[†]Laboratory of Optical Materials and Structures, Rzhanov Institute of Semiconductor Physics, SB RAS, Novosibirsk 630090, Russia

[‡]Tomsk State University, Tomsk 634050, Russia

[§]Boreskov Institute of Catalysis, SB RAS, 630090 Novosibirsk, Russia

[∥]Physical Department, Novosibirsk State University, 630090 Novosibirsk, Russia

[⊥]Laboratory of Crystal Chemistry, Nikolaev Institute of Inorganic Chemistry, SB RAS, 630090 Novosibirsk, Russia

[#]Laboratory of Silicon Material Science, Rzhanov Institute of Semiconductor Physics, SB RAS, 630090 Novosibirsk, Russia

Supporting Information

ABSTRACT: Polycrystalline α-GeO_2, space group $P3_221$, has been prepared by low-temperature chemical synthesis. α-GeO_2 electronic structure has been evaluated comparatively by X-ray photoelectron spectroscopy (XPS) and ab initio calculations. The oxygen vacancies have been formed in α-GeO_2 by Ar^+ ion bombardment at ion energy 2.4 keV. The appearance of oxygen-vacancy-induced new states in the band gap has been detected by XPS and theoretical analysis. It has been shown that oxygen monovacancy generation provides defect states in the valence band, in the band gap, and in the conduction band.

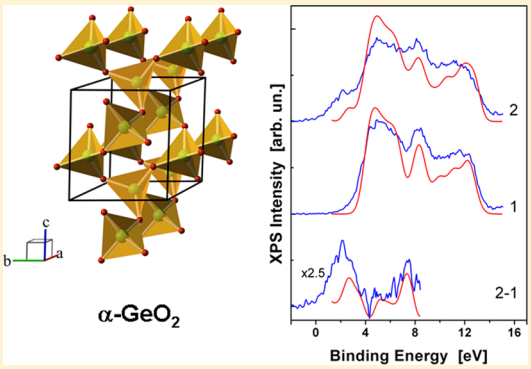

1. INTRODUCTION

Germanium dioxide (GeO_2 or germania) has been the focus of many investigations over the recent years because this oxide is a key constituent in optical fibers, microelectronic and micro-photonic structures, and luminescence compounds.[1−8] In microelectronics, GeO_2 is the important thin-film insulator material for the applications in the Ge-based device structures similar to SiO_2 in the Si-based MOS technology because the germanium oxide layer exists even at high-k oxide/Ge interfaces.[3,9−12] Presently, GeO_2 is being intensively explored as a functional dielectric material in memristor devices based on the resistance switching effect.[7,13]

It is well-known that electronic parameters of dielectric oxide materials are strongly dependent on stoichiometry, and oxygen loss commonly generates new states in the band gap with a drastic conductivity variation.[14−18] As for GeO_2, the defect formation appears in the reduced atmosphere, and this process is sensitive to the initial phase composition of the oxide.[19] Similar oxygen vacancy generation effects can be reasonably supposed in the vacuum environment, and this possibility should be considered in the design of device structures. The influence of oxygen deficiency on GeO_2 properties is not clear in detail. Recently, however, it has been shown by theoretical methods that the α-quartz-type GeO_2 (α-GeO_2) vibrational parameters are very sensitive to the presence of the vacancy in the oxygen sublattice.[20] This polymorph modification is particularly interesting because α-GeO_2, space group $P3_121$ or $P3_221$, possesses a wide optical transparency range and piezoelectric and nonlinear optical properties.[4,21−23] The α-GeO_2 crystal structure is shown in Figure 1.[24,25] During recent years, the α-GeO_2 crystal flux growth technology has been developed, and now large, free of hydroxyl groups, high-stability single crystals are available.[23,26,27] Thus, the present study is aimed at the evaluation of α-GeO_2 electronic structure. The electronic parameters are planned to be explored in parallel by experimental and theoretical methods. This algorithm is helpful for the selection of optimal approximations in band structure calculations and for the accurate evaluation of electronic structure impacted by the oxygen vacancy formation.[28−31]

2. EXPERIMENTAL SECTION

The α-GeO_2 crystals were prepared by low-temperature chemical synthesis from the crystalline GeO_2 powder of optical grade (Umicore Electro-optic Materials) using aqueous ammonia (20.27 wt %), nitric acid (69.23 wt %), and distilled water.[4,32] The 0.2 g of powder was placed into a beaker which

Received: November 30, 2013
Revised: January 16, 2014
Published: January 29, 2014

 © 2014 American Chemical Society dx.doi.org/10.1021/jp411751c | J. Phys. Chem. C 2014, 118, 3644−3650

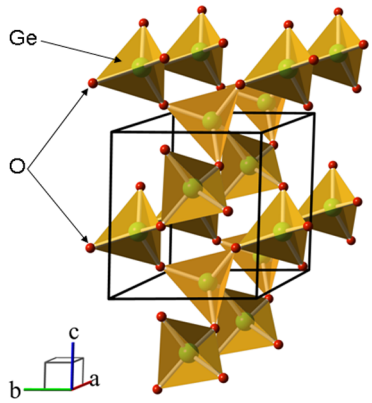

Figure 1. Crystal structure of α-GeO_2. The unit cell is outlined. Lone germanium and oxygen atoms are omitted for clarity.

was then filled up with 50 mL of distilled water. The mixture was heated to 90 °C under magnetic stirring, and then 1.6 mL of ammonia was added to achieve pH = 10. After that, 5 mL of nitric acid was added into the precursor solution; hereupon, it was evaporated down to the 10 mL volume, up to a moment when the white powder was abundantly precipitated. Under the conditions, the reaction between crystalline germanium dioxide and aqueous ammonia produces a precursor solution with concentration of GeO_2 of 0.033 mol/L. The concentration is favorable to get the monomeric germanate anions in the aqueous solution.[33] After the fast change of pH from 10 to 1 via nitric acid addition, the GeO_2 solubility strongly decreases. The process causes a heterogeneous nucleation with further crystal growth by the sorption mechanism which is assisted with evaporation. The precipitate was separated by centrifugation and washed, first, with 0.1 mol of HNO_3 solution and then with ethanol repeatedly. The washed product was dried under ambient conditions; then it was heat-treated for 4 h at T = 200 °C under 0.1 Pa vacuum with the Ar flow of 1.2 L/h. The microstructure of final α-GeO_2 powder product was determined by scanning electron microscopy (SEM) using a Hitachi S4800 high-performance machine, and the pattern is shown in Figure 1S (Supporting Information).

Structural properties of germanium oxide were evaluated with X-ray diffraction (XRD) analysis. The XRD pattern was obtained on a Shimadzu XRD-7000 device equipped with a Ni filter using Cu Kα radiation. The diffractograms were recorded with step scans from 5 to 100° in the 2θ angle and 10 s for each 0.02° step. The unit cell parameters (UCPs) of the detected phase were determined by the full-profile refinement in the 2θ range of 10−100°. The full-profile refinement PowderCell 2.4 program was used for the calculations;[34] the peaks were described by the pseudo-Voigt function.

The XPS measurements were performed on an X-ray photoelectron spectrometer (SPECS Surface Nano Analysis GmbH) equipped with an X-ray source XR-50 M with a double Al/Ag anode, an ellipsoidal crystal X-ray monochromator FOCUS-500, a PHOIBOS-150-MCD-9 hemispherical electron energy analyzer, and an ion source IQE-11.[35,36] The spectra were obtained using monochromatic Al Kα radiation at the fixed analyzer pass energy of 20 eV under the ultrahigh vacuum conditions. For charge compensation, a low voltage electron flood gun FG-20 was used, and the precise charge correction was performed by setting the Ge $2p_{3/2}$ peak at the binding energy (BE) of 1220.4 eV. The high concentration of oxygen vacancies in the GeO_2 crystal lattice was generated by Ar^+ ion bombardment at the ion energy of 2.4 keV and a current density of approximately 10 $\mu A/cm^2$.[37,38]

3. COMPUTATIONAL METHODS

The higher-level electronic-structure calculations were performed using the density functional theory (DFT) with an exact exchange contribution calculated by the Hartree−Fock method, i.e., B3LYP hybrid functionals.[39] The B3LYP exchange-correlation functional well reproduces the band gaps of transition metal oxides and is most suitable for our purposes. The calculations were made using the following electronic configuration of the constituent elements: Ge [Ar $3d^{10}$] $4s^2$ $4p^2$ and O [He] $2s^2$ $2p^4$, where the core configurations are shown in the parentheses. The potentials of nuclei and core electrons were expressed via preliminarily generated atomic pseudopotentials retaining the norm.[40] The Bloch functions of electrons in the crystal were represented by plane-wave expansions with the cutoff energy of 60 Ry. The cutoff energy was selected to ensure the convergence of the total cell energy to 0.006 eV/atom. The density of calculation grid in the reciprocal space was 2 × 2 × 2. The atomic arrangement was optimized with the force convergence threshold of 0.04 eV/Å performed within standard DFT. We used a supercell of 72 atoms for the solitary oxygen vacancy simulation and 36 atoms for the simulating of a sufficiently nonstoichiometric germanium oxide. The oxygen vacancy and polyvacancy were generated by the removal of the O atom close to the center of the supercell, followed by remaining atoms relaxation. The theoretical XPS spectra were calculated summing up the partial density of states with the coefficients corresponding to photoionization cross sections.[41] The calculations were performed with the Quantum-ESPRESSO package.[42]

4. RESULTS AND DISCUSSION

As a result of aqua synthesis, the homotypic monodimensional microcrystals with the diameter up to 1 μm are formed as shown in Figure 1S (Supporting Information). XRD analysis of the sample was carried out using the PDF-2 database.[43] Experimental and theoretical diffraction patterns are presented in Figure 2S (Supporting Information). All the diffraction peaks were successfully indexed, and their positions are in good agreement with those of trigonal α-GeO_2, space group $P3_221$. It is evident that the pure α-GeO_2 phase is present in the powder sample. The difference curve is shown in the lower part of Figure 2S (Supporting Information). The unit cell parameters defined from the measured sample (a = 4.986(3), c = 5.652(4) Å) are in excellent relation to the parameters previously reported for pure α-GeO_2 oxide as a = 4.98502 and c = 5.6480 Å.[44]

A. Core Level Photoelectron Spectra. The Ge $2p_{3/2}$ spectra recorded before and after ion bombardment of α-GeO_2 are shown in Figure 2. The peaks are a little asymmetrical, and that complicates their adequate curve fitting into individual components. A small Ge $2p_{3/2}$ peak broadening appeared at long bombardment times. The plasmon oscillation excitation energy was determined on the basis of the Ge $2p_{3/2}$ energy loss spectra analysis (Figure 2). The spectrum of the initial surface contains a wide loss peak at 15.5 eV above the Ge $2p_{3/2}$ peak, whereas the spectra recorded after 2, 20, and 40 min of the surface bombardment exhibit the loss peaks positioned 15.4, 15.7, and 15.6 eV apart, respectively. The values are in reasonable relation to the excitation energy of 16.38 eV found

dx.doi.org/10.1021/jp411751c | J. Phys. Chem. C 2014, 118, 3644−3650

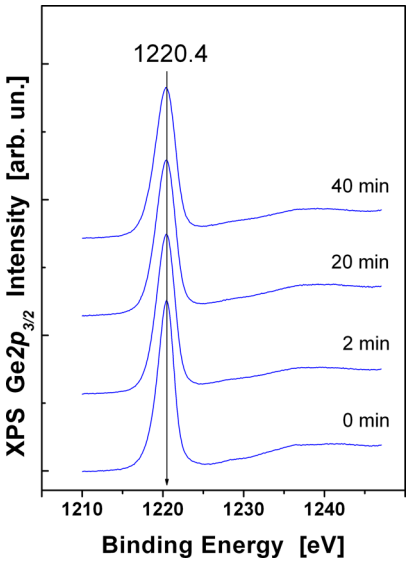

Figure 2. Ge $2p_{3/2}$ core-level spectra recorded from the initial and ion bombarded α-GeO_2 surface.

for the plasmon oscillations in α-GeO_2 by quantum-chemical calculations.[45] The O 1s core level spectra are shown in Figure 3 as a function of ion etching time. A drastic shift of the O 1s

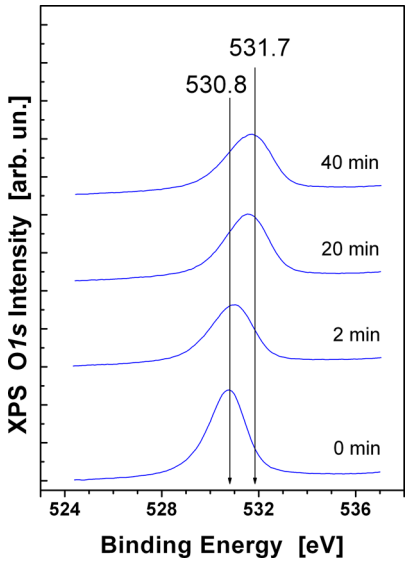

Figure 3. O 1s core-level spectra obtained before and after ion bombardment of α-GeO_2 during 2, 20, and 40 min, respectively.

spectra to the higher binding energy side is observed with an increase in the bombardment times (see details in Table 1). This effect is due to a change of ionicity of the Ge−O bond in germanium oxide. The band gap in α-GeO_2 was estimated using the energy loss spectrum (Figure 3S, Supporting Information) as was proposed earlier.[46,47] According to the previous optical measurements, the band gap in α-GeO_2 is 5.72 eV.[4] In the present XPS experiment, the band gap for perfect α-GeO_2 was estimated to be 5.4 eV, which is similar to the value found earlier in ref 4, whereas, after ion etching, the band gap values lay in the range of 4.4−4.6 eV. All XPS data are summarized in Table 1.

The α-GeO_2 valence band spectra recorded before and after ion bombardment during 2 min are shown in Figure 4. The spectrum can be divided into three regions.[48,50,54−56] The most intense peak at ∼31.4 eV below the Fermi level is mainly due to the photoemission from the Ge 3d level. According to the partial densities of states calculated from the first principles, the features over the range of 29−19 eV are due to the photoemission from the O 2s level, while the features in the region below 19 eV can be attributed to the photoemission from the hybridized levels Ge 4s−Ge 4p−O 2p. The difference spectrum obtained by subtracting spectrum 1 multiplied by a factor ∼0.9 from spectrum 2 is also demonstrated in Figure 4. The difference spectrum indicates broadening of the Ge 3d peak as a result of ion bombardment. Besides, the generation of additional peaks in the region of mixed states in 2 min of etching with Ar^+ ions is clearly seen in the difference spectrum. The ion bombardment leads to the appearance of an additional wide peak at 2.1 eV corresponding to the electron photoemission from defects in the α-GeO_2 structure. A further increase of the ion etching time does not lead to noticeable changes in the valence band spectra. Comparatively, the ion bombardment induces a substantial change in the BE values of the representative element core levels O 1s, Ge 3d, and C 1s, as reported in Table 1.

Since the Ge 3d and Ge $2p_{3/2}$ levels have drastically different energies, this configuration may be used for the characterization of the germanium ion environment at different depths. The BE(Ge $2p_{3/2}$) binding energy is very high, and this photoemission signal is related to the top surface. Contrary to that, the Ge 3d binding energy is low, and the behavior of the peak characterizes the deeper oxide layers. Besides, it is valuable to use BE difference parameters ΔGe_{3d} = BE(O 1s) − BE(Ge 3d) and ΔGe_{2p} = BE (O 1s) − BE(Ge $2p_{3/2}$) for the comparison instead of element binding energies because the BE difference parameters are insensitive to the energy scale calibration method and surface charging effects. Previously, the algorithm was successfully tested for different chemical oxide classes, and the results can be found elsewhere.[15,57−63] The suite of electronic parameters earlier observed by XPS of GeO_2 and those found in the present study at different ion etching times are shown in Table 1. The earlier results found in the literature are related dominantly to the oxide films formed at Ge substrates. The film crystallinity was not analyzed by structural methods; however, the films were prepared at low temperatures, and the GeO_2 oxides can be reasonably considered as being in the amorphous state. Tetragonal GeO_2 has not been evaluated by XPS up to now, and only a unique short report of α-GeO_2 electronic parameters was found in ref 49. In GeO_2 films and glass, parameters ΔGe_{3d} and ΔGe_{2p} are in the ranges of 498.4−498.9 and −(688.7−688.4) eV, respectively. The parameters ΔGe_{3d} = 499.3 and ΔGe_{2p} = −689.7 eV defined in the present study for crystalline α-GeO_2 before ion bombardment are noticeably different from those reported in the literature for GeO_2 films. At longer ion bombardment times, parameter ΔGe_{2p} increases up to −688.75 eV. The value is in good relation to the range that is a characteristic of amorphous GeO_2 films, and this indicates the complete amorphization of the α-GeO_2 particle top surface by ion bombardment. Contrary to that, the variation of ΔGe_{3d} with an increase of ion bombardment time is negligible, and this may signify the persistence of the atomic order, at least partially, in the deeper layers. So, it can be concluded that, most likely, the top surface layer crystallinity is destroyed by ion bombardment, and deeper layers keep the atomic order despite the oxygen vacancy formation.

dx.doi.org/10.1021/jp411751c | J. Phys. Chem. C 2014, 118, 3644−3650

Table 1. Ge 3d, O 1s, Ge $2p_{3/2}$, and C 1s Binding Energies (eV) Observed for Germanium Oxide, as Well as the Differences (O 1s − Ge 3d) and (O 1s − Ge $2p_{3/2}$) between Corresponding Levels

Ge 3d	O 1s	Ge $2p_{3/2}$	C 1s	O 1s − Ge 3d	O 1s − Ge $2p_{3/2}$	oxide state	ref
33.7	-	-	-	-	-	film, radical oxidation	3
33.2	-	-	-	-	-	film, thermal oxidation	11
BE(Ge^0) + 3.3	-	-	-	-	-	film, vacuum oxidation	48
33.7	532.3	-	-	498.6	-	α-GeO_2	49
33.4	532.3	1220.7	-	498.9	−688.4	film, vacuum oxidation	50
33.3	532.2	1220.9	285.3	498.9	−688.7	film, native oxide	51
-	531.7	1220.2	284.6	-	−688.5	GeO_2 glass	52
33.4	531.8	-	-	498.4	-	film, oxidation in the air	53
31.41 (0 min)	530.74	1220.4	283.25	499.3	−689.7	α-GeO_2	present study
31.78 (2 min)	530.94	1220.4	283.78	499.2	−689.5		
32.35 (20 min)	531.54	1220.4	284.46	499.2	−688.78		
32.37 (40 min)	531.65	1220.4	284.36	499.28	−688.75		

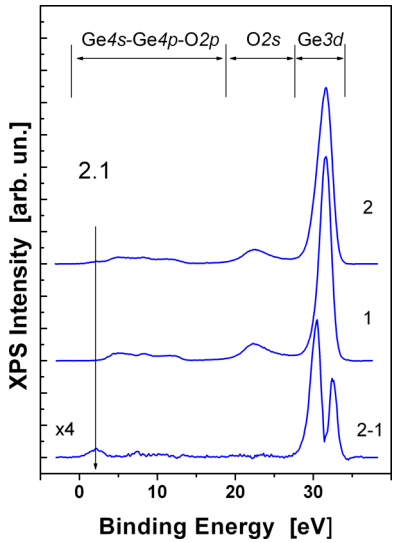

Figure 4. Photoemission spectra of the valence band of α-GeO_2 before (1) and after (2) ion bombardment during 2 min. The difference spectrum (2-1) is shown at the bottom.

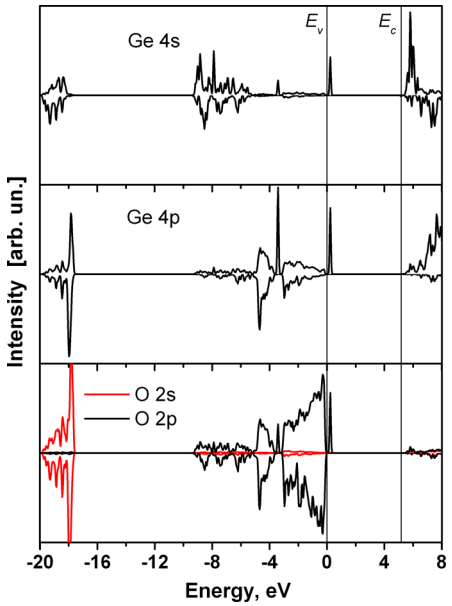

Figure 5. PDOS for the Ge and O atoms nearest to the oxygen vacancy (upper curve) compared with the corresponding spectra for atoms in a defect-free supercell (reversed curve). The top of the valence band is set to zero energy.

B. Electronic Band Structures. The calculated partial density of states (PDOS) for both perfect and defect α-GeO_2 supercells is shown in Figure 5. The PDOS indicates that, in perfect and defect α-GeO_2, the lower subzone −(19.8−17.5) eV of the valence band is formed mainly from the O 2s states, while the upper subzone −(9.3−0.0) eV is formed from the O 2p states. The electronic states of germanium form mostly the conduction band (>5.3 eV), but they also contribute (≈10%) to the states in the valence band. The single-particle band gap of α-GeO_2 obtained in our periodic calculations is 5.3 eV, which is close to the experimental value for the optical gap of 5.72 eV.[4] A defect-free crystal demonstrates a narrow gap in the valence band at −(3.4−3.8) eV, which separates bonding orbitals O 2p−Ge 4s,4p from nonbonding orbitals O $2p_\pi$, similarly to that of α-SiO_2.[64]

The introduction of the oxygen vacancy defect in the α-GeO_2 supercell generates several new features. The presence of the neutral oxygen vacancy in α-GeO_2 leads to the defect levels at −3.28, 0.4, and 5.9 eV. The defect level in the band gap (0.4 eV) is filled with two electrons, which corresponds to a bonding state of the Ge−Ge defect in GeO_2. The level at 5.9 eV near the conduction band bottom corresponds to the nonbonding state of the Ge−Ge bond. The defect levels at −3.28 and 0.4 eV are formed from the states Ge 4s, Ge 4p, and O 2p closest to the vacancy, while the level at 5.9 eV in the continuum spectrum is formed only from germanium states. The small dispersion of defective peaks at −3.28 and 0.4 eV indicates a strong localization in the real space. The valence band photoemission spectra recorded for initial and bombarded samples are shown in Figure 6. For initial α-GeO_2, the mixed states are observed in the range of 3−13 eV with the peaks resolved at ∼5, 8, and 12.3 eV. As it is evident from the curve set (1), the relation between the calculated and measured spectra is very good. The set spectra (2) of a short time bombarded sample are noticeably different due to the new state generation at ∼2 and 5−8 eV, as revealed by the set of difference spectra (2-1). This results in the noticeable band gap lowering. A good agreement between experimental XPS spectra and the spectra calculated from the first principles (Figure 6) verifies the correctness of the theoretical model and elucidates the nature of the defect peak at 2.1 eV. According to the calculated data, the peak at 2.1 eV is considerably due to oxygen polyvacancies. Oxygen monovacancies in α-GeO_x of any stoichiometry do not correspond to

dx.doi.org/10.1021/jp411751c | J. Phys. Chem. C 2014, 118, 3644−3650

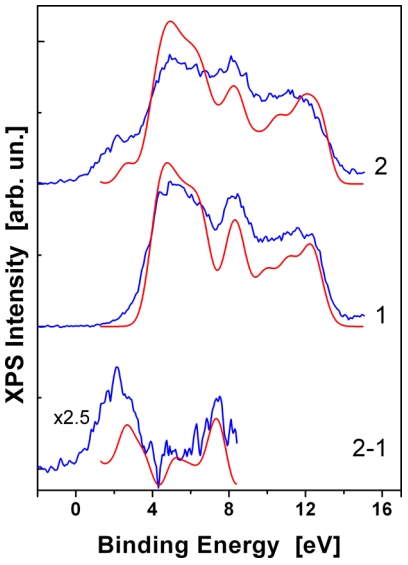

Figure 6. Experimental XPS spectra (blue) of the valence band top before (1) and after (2) ion bombardment during 2 min. The calculated one (red) for perfect α-GeO_2 (1) and for a crystal lattice with oxygen vacancy (2). The difference spectra (2-1) are shown at the bottom. The zero energy (E = 0) is taken as the valence band top of bombarded GeO_2.

this level. The XPS spectrum of nonstoichiometric germanium oxide was simulated using a 36-atom supercell of α-GeO_2, from which four atoms of oxygen bonded with a single germanium atom were removed to create a $GeO_{1.67}$ crystal. The calculated defect level position was at 2.7 eV, and it was sufficiently less intensive than the experimental peak at 2.1 eV.

5. CONCLUSIONS

The comparative exploration of the electronic parameters of noncentrosymmetric α-GeO_2 has been implemented in the present study. The electronic parameters of perfect and oxygen-deficient α-GeO_2 were measured by XPS. The electronic structure of α-GeO_2 with neutral oxygen vacancies and polyvacancies was calculated using the DFT with hybrid functionals, which correctly describes excited states. The calculated band gap of α-GeO_2 is 5.3 eV, which well agrees with the earlier experimental results. The oxygen monovacancy provides defect states in the valence band, in the band gap, and in the conduction band. The comparative analysis performed in this study yields the relation between oxygen vacancy formation and electronic structure variation in α-GeO_2.

■ ASSOCIATED CONTENT

Ⓢ Supporting Information

Includes SEM image, XRD pattern, and O 1s core level measured by XPS. This information is available free of charge via the Internet at http://pubs.acs.org.

■ AUTHOR INFORMATION

Corresponding Author

*Phone: +7 (383) 3308889. Fax: +7 (383) 3332771. E-mail: atuchin@isp.nsc.ru.

Notes

The authors declare no competing financial interest.

■ ACKNOWLEDGMENTS

This work was supported by projects 1.14 of the Siberian Branch of the Russian Academy of Sciences and 24.18 of the Russian Academy of Sciences. V.V.K. gratefully acknowledge the Ministry of Education and Science of the Russian Federation for financial support. The computations have been carried out at the Supercomputer Center of the Novosibirsk State University.

■ REFERENCES

(1) Micoulaut, M.; Cormier, L.; Henderson, G. S. The Structure of Amorphous, Crystalline and Liquid GeO_2. *J. Phys.: Condens. Matter* **2006**, *18*, R753−R784.

(2) Arai, N.; Tsuji, H.; Hattori, M.; Ohsaki, M.; Kotaki, H.; Ishibashi, T.; Gotoh, Y.; Ishikawa, J. Luminescence Properties of Ge Implanted SiO_2:Ge and GeO_2:Ge Films. *Appl. Surf. Sci.* **2009**, *256*, 954−957.

(3) Kobayashi, M.; Thareja, G.; Ishibashi, M.; Sun, Y.; Griffin, P.; McVittie, J.; Pianetta, P.; Saraswat, K.; Nishi, Y. Radical Oxidation of Germanium for Interface Gate Dielectric GeO_2 Formation in Metal-Insulator-Semiconductor Gate Stack. *J. Appl. Phys.* **2009**, *106*, 104117.

(4) Ramana, C. V.; Carbajal-Franco, G.; Vemuri, R. S.; Troitskaia, I. B.; Gromilov, S. A.; Atuchin, V. V. Optical Properties and Thermal Stability of Germanium Oxide (GeO_2) Nanocrystals with α-quartz Structure. *Mater. Sci. Eng., B* **2010**, *174*, 279−284.

(5) Jing, C.; Zhang, C.; Shi, Y.; Chu, J. Attenuated Total Reflection GeO_2 Hollow Waveguide for 9.6−11.7 μm Infrared Light Transmission. *Appl. Phys. Lett.* **2011**, *99*, 161107.

(6) Jawad, M. J.; Hashim, M. R.; Ali, N. K. Synthesis, Structural, and Optical Properties of Electrochemically Deposited GeO_2 on Porous Silicon. *Electrochem. Solid State Lett.* **2011**, *14*, D17−D19.

(7) Shaposhnikov, A. V.; Perevalov, T. V.; Gritsenko, V. A.; Chen, C. H.; Chin, A. Mechanism of GeO_2 Resistive Switching Based on the Multi-Phonon Assisted Tunneling between Traps. *Appl. Phys. Lett.* **2012**, *100*, 243506.

(8) Shinde, S. L.; Nanda, K. K. Towards the Understanding of Formation of Micro/Nano Holes of Ge/GeO_2 through Phase Mapping. *CrystEngComm* **2013**, *15*, 4049−4053.

(9) Lee, C. H.; Tabata, T.; Nishimura, T.; Nagashio, K.; Kita, K.; Toriumi, A. Ge/GeO_2 Interface Control with High-Pressure Oxidation for Improving Electrical Characteristics. *Appl. Phys. Express* **2009**, *2*, 071404.

(10) Ramana, C. V.; Troitskaia, I. B.; Gromilov, S. A.; Atuchin, V. V. Electrical Properties of Germanium Oxide with α-quartz Structure Prepared by Chemical Precipitation. *Ceram. Int.* **2012**, *38*, 5251−5255.

(11) Zhang, W. F.; Nishimura, T.; Nagashio, K.; Kita, K.; Toriumi, A. Conduction Band Offset at GeO_2/Ge Interface Determined by Internal Photoemission and Charge-Corrected X-ray Photoelectron Spectroscopies. *Appl. Phys. Lett.* **2013**, *102*, 102106.

(12) Ma, J.; Zhang, J. F.; Ji, Z.; Benbakhti, B.; Duan, M.; Zhang, W.; Zheng, X. F.; Mitard, J.; Kaczer, B.; Groeseneken, G.; Hall, S.; Robertson, J.; Chalker, P. Towards Understanding Hole Traps and NBTI of Ge/GeO_2/Al_2O_3 Structure. *Microelectron. Eng.* **2013**, *109*, 43−45.

(13) Lin, T.-S.; Lou, L.-R.; Lee, C.-T.; Tsai, T.-C. Memory Characteristics of Metal-Oxide-Semiconductor Structures Based on Ge Nanoclusters-Embedded GeO_x Films Grown at Low Temperature. *J. Nanosci. Nanotechnol.* **2012**, *12*, 2076−2080.

(14) Robertson, Interfaces and Defects of High-*k* Oxides on Silicon. *J. Solid-State Electronics* **2005**, *49*, 283-293.

(15) Shvets, V. A.; Aliev, V. Sh.; Gritsenko, D. V.; Shaimeev, S. S.; Fedosenko, E. V.; Rykhlitski, S. V.; Atuchin, V. V.; Gritsenko, V. A.; Tapilin, V. M.; Wong, H. Electronic Structure and Charge Transport Properties of Amorphous Ta_2O_5 Films. *J. Non-Cryst. Solids* **2008**, *354*, 3025−3033.

(16) Quah, H. J.; Cheong, K. Y. Deposition and Post-Deposition Annealing of Thin Y_2O_3 Film on n-type Si in Argon Ambient. *Mater. Chem. Phys.* **2011**, *130*, 1007−1015.

(17) Pustovarov, V. A.; Perevalov, T. V.; Gritsenko, V. A.; Smirnova, T. P.; Yelisseyev, A. P. Oxygen Vacancy in Al_2O_3: Photoluminescence Study and First-Principle Simulation. *Thin Solid Films* **2011**, *519*, 6319−6322.
(18) Sze, S. M. The Floating-Gate Non-Volatile Semiconductor Memory − from Invention to the Digital Age. *J. Nanosci. Nanotechnol.* **2012**, *12*, 7587−7596.
(19) Bielz, T.; Soisuwan, S.; Girgsdies, F.; Klötzer, B.; Penner, S. Reduction of Different GeO_2 Polymorphs. *J. Phys. Chem. C* **2012**, *116*, 9961−9968.
(20) Kislov, A. N.; Zatsepin, A. F. Vibrations Induced by Different Charged Oxygen Vacancies in Quartz-Like GeO_2. *Comput. Mater. Sci.* **2013**, *74*, 12−16.
(21) Balitskii, D. B.; Sil'verstova, O. Yu.; Balitskii, V. S.; Pisarevskii, Yu. V.; Pushcharovskii, D. Yu.; Philippot, E. Elastic, Piezoelectric, and Dielectric Properties of α-GeO_2 Single Crystals. *Cryst. Rep.* **2000**, *45*, 145−147.
(22) Atuchin, V. V.; Kidyarov, B. I.; Troitskaia, I. B. Interrelationship of Micro- and Macrostructure with Physical Properties of Non-centrosymmetric Germanates. *Ferroelectrics* **2013**, *444*, 137−143.
(23) Lignie, A.; Ménaert, B.; Armand, P.; Peña, A.; Debray, J.; Papet, P. Top Seeded Solution Growth and Structural Characterizations of α-Quartz-Like Structure GeO_2 Single Crystal. *Cryst. Growth Des.* **2013**, *13* (10), 4220−4225.
(24) Glinnemann, J.; King, H. E.; Schulz, H.; la Placa, S. J.; Dacol, F. Crystal Structures of the Low-Temperature Quartz-Type Phases of SiO_2 and GeO_2 at Elevated Pressure. *Z. Kristallogr.* **1992**, *198*, 177−212.
(25) Ozawa, T. C.; Kang, S. J. Balls&Sticks: Easy-to-Use Structure Visualization and Animation Program. *J. Appl. Crystallogr.* **2004**, *37*, 679.
(26) Lignie, A.; Armand, P.; Papet, P. Growth of Piezoelectric Water-Free GeO_2 and SiO_2-Substituted GeO_2 Single-Crystals. *Inorg. Chem.* **2011**, *50*, 9311−9317.
(27) Lignie, A.; Granier, D.; Armand, P.; Haines, J.; Papet, P. Modulation of Quartz-Like GeO_2 Structure by Si Substitution: an X-ray Diffraction Study of $Ge_{1-x}Si_xO_2$ ($0 \le x \le 0.2$) Flux-Grown Single Crystals. *J. Appl. Crystallogr.* **2012**, *45*, 272−278.
(28) Khyzhun, O. Yu.; Bekenev, V. L.; Atuchin, V. V.; Sinelnichenko, A. K.; Isaenko, L. I. Electronic Structure of $KTiOAsO_4$: A Comparative Study by the Full Potential Linearized Augmented Plane Wave Method, X-ray Emission Spectroscopy and X-ray Photoelectron Spectroscopy. *J. Alloys Compd.* **2009**, *477*, 768−775.
(29) Atuchin, V. V.; Isaenko, L. I.; Kesler, V. G.; Lobanov, S.; Huang, H.; Lin, Z. S. Electronic Structure of $LiGaS_2$. *Solid State Commun.* **2009**, *149*, 572−575.
(30) Atuchin, V. V.; Isaenko, L. I.; Kesler, V. G.; Lin, Z. S.; Molokeev, M. S.; Yelisseyev, A. P.; Zhurkov, S. A. Exploration on Anion Ordering, Optical Properties and Electronic Structure in $K_3WO_3F_3$ Elpasolite. *J. Solid State Chem.* **2012**, *187*, 159−164.
(31) Khyzhun, O. Y.; Bekenev, V. L.; Atuchin, V. V.; Galashov, E. N.; Shlegel, V. N. Electronic Properties of $ZnWO_4$ Based on ab initio FP-LAPW Band-Structure Calculations and X-ray Spectroscopy Data. *Mater. Chem. Phys.* **2013**, *140*, 588−595.
(32) Atuchin, V. V.; Gavrilova, T. A.; Gromilov, S. A.; Kostrovsky, V. G.; Pokrovsky, L. D.; Troitskaia, I. B.; Vemuri, R. S.; Carbajal-Franco, G.; Ramana, C. V. Low-Temperature Chemical Synthesis and Microstructure Analysis of GeO_2 Crystals with α-Quartz Structure. *Cryst. Growth Des.* **2009**, *9*, 1829−1832.
(33) Rimer, J. D.; Roth, D. D.; Vlachos, D. G.; Lobo, R. F. Self-Assembly and Phase Behavior of Germanium Oxide Nanoparticles in Basic Aqueous Solutions. *Langmuir* **2007**, *23*, 2784−2791.
(34) Kraus, W.; Nolze, G. *POWDER CELL* - a Program for the Representation and Manipulation of Crystal Structures and Calculation of the Resulting X-ray Powder Patterns. *J. Appl. Crystallogr.* **1996**, *29*, 301−303.
(35) Ramana, C. V.; Vemuri, R. S.; Kaichev, V. V.; Kochubey, V. A.; Saraev, A. A.; Atuchin, V. V. X-ray Photoelectron Spectroscopy Depth Profiling of La_2O_3/Si Films Deposited by Reactive Magnetron Sputtering. *ACS Appl. Mater. Interfaces* **2011**, *3*, 4370−4373.
(36) Yakovkina, L. V.; Smirnova, T. P.; Borisov, V. O.; Kichai, V. N.; Kaichev, V. V. Synthesis and Properties of Dielectric $(HfO_2)_{1-x}(Sc_2O_3)_x$ Films. *Inorg. Mater.* **2013**, *49*, 172−178.
(37) Ivanov, M. V.; Perevalov, T. V.; Aliev, V. Sh.; Gritsenko, V. A.; Kaichev, V. V. Ab initio Simulation of the Electronic Structure of delta-Ta_2O_5 with Oxygen Vacancy and Comparison with Experiment. *J. Exp. Theor. Phys.* **2011**, *112*, 1035−1041.
(38) Ivanov, M. V.; Perevalov, T. V.; Aliev, V. S.; Gritsenko, V. A.; Kaichev, V. V. Electronic Structure of delta-Ta_2O_5 with Oxygen Vacancy: ab initio Calculations and Comparison with Experiment. *J. Appl. Phys.* **2011**, *110*, 024115.
(39) Giannozzi, P.; Baroni, S.; Bonini, N.; et al. QUANTUM ESPRESSO: a Modular and Open-Source Software Project for Quantum Simulations of Materials. *J. Phys.: Condens. Matter* **2009**, *21*, 395502.
(40) Perdew, J.; Burke, K.; Ernzerhof, M. Rationale for Mixing Exact Exchange with Density Functional Approximations. *J. Chem. Phys.* **1996**, *105*, 9982−9985.
(41) Yeh, J. J. *Atomic Calculation of Photoionization Cross-Section and Asymmetry Parameters*; Gordon and Breach Science Publisher: Amsterdam, 1993.
(42) Troullier, N.; Martins, J. L. Efficient Pseudopotentials for Plane-Wave Calculations. *Phys. Rev. B* **1991**, *43*, 1993−2006.
(43) Powder Diffraction File. *Inorganic Phases*; International Centre for Diffraction Data: Pennsylvania, USA, 2010.
(44) Smith, G.; Isaacs, P. The Crystal Structure of Quartz-Like GeO_2. *Acta Crystallogr.* **1964**, *17*, 842−846.
(45) Ravindra, N. M.; Weeks, R. A.; Kinser, D. L. Optical Properties of GeO_2. *Phys. Rev. B* **1987**, *36*, 6132−6134.
(46) Nohira, H.; Tsai, W.; Besling, W.; Young, E.; Petry, J.; Conard, T.; Vandervorst, W.; De Gendt, S.; Maes, J.; Tuominen, M. Characterization of ALCVD-Al_2O_3 and ZrO_2 Layer Using X-ray Photoelectron Spectroscopy. *J. Non-Cryst. Solids* **2002**, *303*, 83−87.
(47) Perevalov, T. V.; Gritsenko, V. A.; Kaichev, V. V. Electronic Structure of Aluminum Oxide: ab initio Simulations of Alpha and Gamma Phases and Comparison with Experiment for Amorphous Films. *Eur. Phys. J. Appl. Phys.* **2010**, *52*, 30501.
(48) Schmeisser, D.; Schnell, R. D.; Bogen, A.; Himpsel, F. J.; Rieger, D.; Landgren, G.; Morar, J. F. Surface Oxidation States of Germanium. *Surf. Sci.* **1986**, *172*, 455−465.
(49) Sorokina, S.; Dikov, Yu. Structural Investigation of the $(Si_{1-x}Ge_x)O_2$ Single Crystal Thin Films by X-ray Photoelectron Spectroscopy. *Proc. SPIE* **1991**, *1519*, 128−133.
(50) Prabhakaran, K.; Ogino, T. Oxidation of Ge(100) and Ge(111) Surfaces: an UPS and XPS Study. *Surf. Sci.* **1995**, *325*, 263−271.
(51) Gabás, M.; Palanco, S.; Bijani, S.; Barrigón, E.; Algora, C.; Rey-Stolle, I.; García, I.; Ramos-Barrado, J. R. Analysis of the Surface State of Epi-Ready Ge Wafers. *Appl. Surf. Sci.* **2012**, *258*, 8166−8170.
(52) Ren, J.; Eckert, H. Quantification of Short and Medium Range Order in Mixed Network Former Glasses in the System GeO_2-$NaPO_3$: A Combined NMR and X-ray Photoelectron Spectroscopy Study. *J. Phys. Chem. C* **2012**, *116*, 12747−12763.
(53) Mura, A.; Hideshima, I.; Liu, Z.; Hosoi, T.; Watanabe, H.; Arima, K. Water Growth on GeO_2/Ge(100) Stack and Its Effect on the Electronic Properties of GeO_2. *J. Phys. Chem. C* **2013**, *117*, 165−171.
(54) Yang, M.; Wu, R. Q.; Chen, Q.; Deng, W. S.; Feng, Y. P.; Chai, J. W.; Pan, J. S.; Wang, S. J. Impact of Oxide Defects on Band Offset at GeO_2/Ge Interface. *Appl. Phys. Lett.* **2009**, *94*, 142903.
(55) Dimoulas, A.; Brunco, D. P.; Rerrari, S.; Seo, J. W.; Panayiotatos, Y.; Sotiropoulos, A.; Conard, T.; Caymax, M.; Spiga, S.; Fanciulli, M.; Dieker, Ch.; Evangelou, E. K.; Galata, S.; Houssa, M.; Heyns, M. M. Interface Engineering for Ge Metal-Oxide-Semiconductor Devices. *Thin Solid Films* **2007**, *515*, 6337−6343.
(56) Liu, Q.-J.; Liu, Z.-T.; Feng, L.-P.; Tian, H. First-Principles Study of Structural, Elastic, Electronic and Optical Properties of Rutile GeO_2 and α-Quartz GeO_2. *Solid State Sci.* **2010**, *12*, 1748−1755.

(57) Atuchin, V. V.; Kalabin, I. E.; Kesler, V. G.; Pervukhina, N. V. Nb 3d and O 1s Core Levels and Chemical Bonding in Niobates. *J. Electron Spectrosc. Relat. Phenom.* **2005**, *142*, 129−134.
(58) Atuchin, V. V.; Kesler, V. G.; Pervukhina, N. V.; Zhang, Z. Ti 2p and O 1s Core Levels and Chemical Bonding in Titanium-Bearing Oxides. *J. Electron Spectrosc. Relat. Phenom.* **2006**, *152*, 18−24.
(59) Atuchin, V. V.; Kesler, V. G.; Pervukhina, N. V. Electronic and Structural Parameters of Phosphorus-Oxygen Bonds in Inorganic Phosphate Crystals. *Surf. Rev. Lett.* **2008**, *15*, 391−399.
(60) Atuchin, V. V.; Isaenko, L. I.; Khyzhun, O. Yu.; Pokrovsky, L. D.; Sinelnichenko, A. K.; Zhurkov, S. A. Structural and Electronic Properties of the $KTiOAsO_4$(001) Surface. *Opt. Mater.* **2008**, *30*, 1149−1152.
(61) Atuchin, V. V.; Galashov, E. N.; Khyzhun, O. Yu.; Kozhukhov, A. S.; Pokrovsky, L. D.; Shlegel, V. N. Structural and Electronic Properties of $ZnWO_4$(010) Cleaved Surface. *Cryst. Growth Des.* **2011**, *11*, 2479−2484.
(62) Atuchin, V. V.; Zhang, Z. Chemical Bonding between Uranium and Oxygen in U^{6+}-containing Compounds. *J. Nucl. Mater.* **2012**, *420*, 222−225.
(63) Atuchin, V. V.; Isaenko, L. I.; Kesler, V. G.; Kang, L.; Lin, Z. S.; Molokeev, M. S.; Yelisseyev, A. P.; Zhurkov, S. A. Structural, Spectroscopic, and Electronic Properties of Cubic G0-Rb_2KTiOF_5 Oxyfluoride. *J. Phys. Chem. C* **2013**, *117*, 7269−7278.
(64) Chelikowsky, J. R.; Schlüter, M. Electron States in α-Quartz: A Self-Consistent Pseudopotential Calculation. *Phys. Rev. B* **1977**, *15*, 4020−4029.